*metals*

MDPI

*Article*

# Creep Deformation Behavior, Microstructure Evolution, and Damage Mechanism of Super304H ODS Steel

**Wan Zhu [1], Zeyue Zhang [2], Dijun Long [3,*], Huijun Li [1] and Liming Yu [1,*]**

[1] State Key Lab of Hydraulic Engineering Simulation and Safety, Tianjin Key Lab of Composite and Functional Materials, Tianjin University, Tianjin 300072, China
[2] Tianjin Walkman Biomaterial Co., Ltd., Tianjin 300000, China
[3] Science and Technology on Reactor Fuel and Materials Laboratory, Nuclear Power Institute of China, Chengdu 610041, China
* Correspondence: djlong1973@163.com (D.L.); lmyu@tju.edu.cn (L.Y.)

**Abstract:** In this paper, the creep deformation behavior, microstructure evolution, and damage mechanism of Super304H oxide dispersion strengthened (ODS) steel have been systematically investigated at 650 °C. The creep behavior of the ODS steel could be understood by virtue of a dislocation creep deformation mechanism. Interrupted creep experiments under 100 MPa were conducted to further study the microstructure evolution during long-term creep deformation. The grains began to refine at the initial stage, and some $M_{23}C_6$ phases were observed at grain boundaries, which enhanced the microhardness during the first creep stage. Along with creep, both $Y_2O_3$ and Cu-rich precipitates exhibited good coherence with the matrix. The $Y_2O_3$ precipitates showed better thermal stability than the Cu-rich phase. During the second creep stage, some cavities emerged around the $M_{23}C_6$ phase and at grain boundaries. The cavities gradually developed into significant cracks, causing the steel to fracture. The creep damage due to cavity growth could be determined according to the creep damage tolerance factor value.

**Keywords:** austenitic ODS steels; long-term creep; microstructure evolution; precipitation; creep cavity

check for updates

**Citation:** Zhu, W.; Zhang, Z.; Long, D.; Li, H.; Yu, L. Creep Deformation Behavior, Microstructure Evolution, and Damage Mechanism of Super304H ODS Steel. *Metals* **2023**, *13*, 1106. https://doi.org/10.3390/met13061106

Academic Editors: Babak Shalchi Amirkhiz and Alireza Akhavan-Safar

Received: 17 April 2023
Revised: 8 June 2023
Accepted: 9 June 2023
Published: 12 June 2023

**Copyright:** © 2023 by the authors. Licensee MDPI, Basel, Switzerland. This article is an open access article distributed under the terms and conditions of the Creative Commons Attribution (CC BY) license (https://creativecommons.org/licenses/by/4.0/).

## 1. Introduction

Super304H austenitic steel is one of the most advanced 18-8 austenitic heat-resistant steels, and has been widely used in ultra-supercritical (USC) power plants because of its admirable creep and oxidation resistance at elevated temperatures [1,2]. Compared to conventional TP304H steel, Super304H steel is additionally alloyed with about 3 wt.% Cu, 0.45 wt.% Nb, and a small amount of N [3–5]. Cu-rich phases, $M_{23}C_6$ carbides, and MX (Nb(C, N)) phases are the predominant precipitates in Super304H stainless steel, and its dominant strengthening effect is derived from the coherent precipitation of nano-sized Cu-rich phases [6]. Jiang et al. reported that, during short-term aging at 650 °C, the yield strength of Super304H steel could be significantly improved by the precipitation hardening effect of the Cu-rich phases [7]. In addition, MX particles with a FCC structure displayed excellent thermal stability, which could make a more durable contribution to the creep strength at high temperatures [8].

However, as the temperature of the working steam and the pressure of the thermal power unit in USC power plants reach approximately 600–650 °C and 25–30 MPa, respectively [9,10], the application of Super304H steel has been seriously limited, due to its deteriorated creep strength at elevated temperatures, such as the sharp decline of impact toughness caused by the rapidly coarsening $M_{23}C_6$ carbides at boundaries [11]. On the contrary, ODS steels have outstanding creep strength at high temperatures, owing to the addition of nano-sized $Y_2O_3$-strengthening particles, which exhibit a remarkable strengthening effect and low coarsening rate, thus obviously preventing the growth of grains by impeding grain boundary migration and dislocation motion [12–14]. Hence, a

novel nano-oxide dispersion strengthening strategy has been proposed for the fabrication of heat-resistant austenite steels. Leo et al. demonstrated that the addition of 0.35 wt.% $Y_2O_3$ to 316L steel could result in a significant increase in yield strength, which was 1.5 times that of the conventional 316L steel at room temperature and twice that at 650 °C [15]. Zhao et al. found that the excellent ductility of ODS steels can be attributed to the bimodal structures and the uniformly dispersed $Y_2Ti_2O_7$ particles [16]. Especially, for the Super304H austenitic ODS steel, a wrapping structure of Cu-rich phases surrounded by Y-rich phases was obtained, which was revealed to bring a more than 50% improvement of the tensile properties at both room and high temperatures [17]. In fact, the creep deformation behavior of austenitic stainless steel and its microstructure evolution during the creep process have been extensively reported, such as creep properties of ODS 316L steel and the effect of precipitating characteristics on the creep behavior of HR3C steel [18]. But, as it is widely applied in extremely harsh environments involving high temperatures and pressures, the creep deformation, microstructure evolution, and damage mechanism of Super304H ODS steel at elevated temperatures have rarely been systematically investigated, which may cause possible danger and economic loss in its practical applications. Therefore, it is necessary to investigate the creep response of Super304H ODS steel at high temperatures.

In this work, the Super304H austenitic ODS steel alloyed with 0.35 wt.% $Y_2O_3$ was prepared through mechanical alloying (MA) and subsequent hot isostatic pressing (HIP) consolidation. A series of creep tests were carried out at 650 °C, with stress levels ranging from 100 to 300 MPa, to investigate the creep deformation behavior of the steel. Interrupted creep experiments were performed under 100 MPa at 650 °C to further explore the microstructure evolution during different creep stages. In addition, the creep damage forms were analyzed.

## 2. Experimental

### *2.1. Material Preparation*

The Super304H austenitic ODS steel was fabricated by the method of powder metallurgy. The pre-alloyed austenitic steel powder was composed of atomized Super304H stainless steel powder and 0.35 wt.% $Y_2O_3$ powder. The chemical compositions of the standard Super304H and the used steel are shown in Table 1. The MA process of the powder mixture was conducted in a QM2SP12 planetary ball mill under a pure Ar atmosphere, with a rotation speed of 200 rpm, a milling time of 48 h, and a ball-to-powder ratio of 6:1. Then, the as-milled powder was degassed within a mold at 500 °C until the vacuum was less than 0.01 Pa. The subsequent consolidation by hot isostatic pressing was conducted at 1150 °C for 3 h under a pressure of 120 MPa. To avoid residual stress during the HIP process, the sinter ingot was gradually cooled to 200 °C in the furnace; then, the pressure was slowly lower to standard atmosphere pressure.

**Table 1.** Chemical compositions of Super304H stainless steel and the as-HIPed ODS steel (wt.%).

| Elements | Fe | Cr | Ni | Si | Mn | Cu | Nb | N | C | Y | O |
|---|---|---|---|---|---|---|---|---|---|---|---|
| Super304H | Bal. | 18.0 | 8.0 | 0.2 | 0.8 | 3.0 | 0.4 | 0.1 | 0.1 | -- | -- |
| Super304H ODS | Bal. | 18.4 | 8.6 | 0.57 | 0.64 | 3.06 | 0.34 | 0.108 | 0.106 | 0.416 | 0.233 |

### *2.2. Creep Tests*

Creep tests for all samples were conducted at 650 °C in an RDL-50 electronic creep machine [19]. Before loading, all specimens were kept at 650 °C for about 1 h to ensure temperature accuracy, and the temperature fluctuation range was controlled within ±2 °C. As shown in Figure 1, the creep specimens were processed into a round shape, with a diameter of 5 mm and a gauge length of 25 mm. The experimental design adheres strictly to the dimensions mandated by the standard of GB/T 2039-2012. On account of the boss existence in the end gauge part, the diameter between the gripping and the gauge part is required to be 10% larger than that of the gauge diameter (5 mm) during the

machined process, which is to ensure that the creep fracture occurs within the designated gauge length.

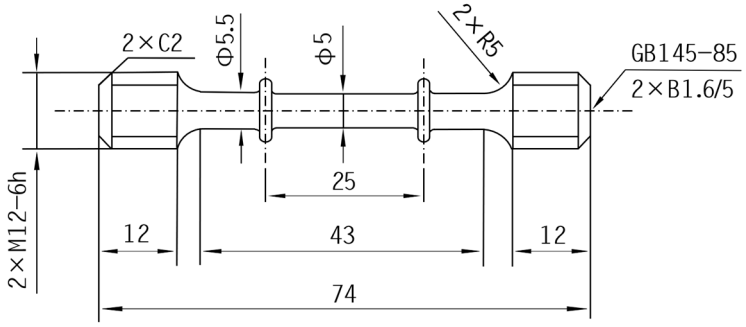



**Figure 1.** Geometrical shape of the creep specimens.

As can be seen in Figure 2, the Super304H ODS steel exhibited relatively high strength at room temperature, and, when tested at 650 °C, its ultimate tensile strength and yield strength were 478 ± 7 and 384 ± 5 MPa, respectively. In general, the half yield stress represents the critical value at which elastic deformation (low-stress regime) transforms into plastic deformation (high-stress regime) [20]. Therefore, in this study, the stress level was ranged from 100 MPa to 300 MPa to cover the whole deformation scope, which was set according to the half value of yield strength at 650 °C (~195 MPa) of the steel.

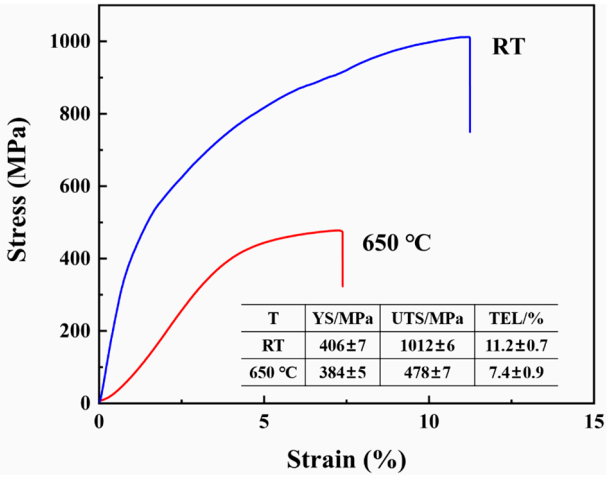



**Figure 2.** Tensile curves of Super304H ODS steel tested at room temperature and 650 °C, respectively.

### *2.3. Microstructure Observation and Analysis*

The creep rupture specimens for observation were cut near the fracture position, while the interrupted samples were taken from their gauge part. A field emission scanning electron microscope (FE-SEM, JSM-7800F), equipped with an electron backscattered diffraction (EBSD) system, was employed to observe creep damage features and analyze the evolution of grains. The SEM samples were mechanically polished and then etched with HCl-$CuCl_2$ solution for 40 s. The samples for EBSD were prepared by argon ion polishing on a Gatan 691 ion thinning instrument and scanned along the stress direction by an EDAX Hikari camera with a step size of 0.05 μm. The collected data were analyzed using OIM 7.2.1 software. The detailed microstructure of the as-HIPed sample and creep samples were characterized by a transmission electron microscope (TEM, FEI Tecnai G2 F30), equipped with an energy dispersive spectroscopy (EDS). High-resolution transmission electron microscope (HRTEM) and high-angle annular dark-field-scanning transmission electron microscope (HAADF-STEM) images were employed to identify the specific structure of nanoparticles. The foil TEM samples were manually thinned to 30 μm in thickness and were then twin-jet

electro-polished in a mixed solution of 10% perchloric acid and 90% ethanol. More than 100 particles in 10 TEM images were counted through Image Pro-Plus 6.0 software, so as to evaluate the evolution of particle diameter and number density.

The microhardness was measured as a supplement to analyze the strength evolution during long-term creep. For each sample, the microhardness was measured five times on a Tukon 2100B Vickers hardness tester, with an applied load of 0.2 kg and a dwelling time of 10 s.

## 3. Results and Discussion

### *3.1. Initial Microstructure of the As-HIPed Sample before Creep*

Figure 3 depicts the microstructure of the as-HIPed austenitic steel. The austenite matrix is composed of equiaxed grains, which can be divided into the ultrafine grain (UFG) zone and coarse grain (CG) zone, as marked in Figure 3a. The size of coarse grains ranges from 1 to 4 μm, while that of most ultrafine grains are less than 400 nm. Such a distribution of grain size is typical in ODS steels after HIP sintering, which can induce back stress to the matrix, due to the non-uniform yield between the UFG zone and CG zone, contributing to the superior strength of ODS steels [21,22].

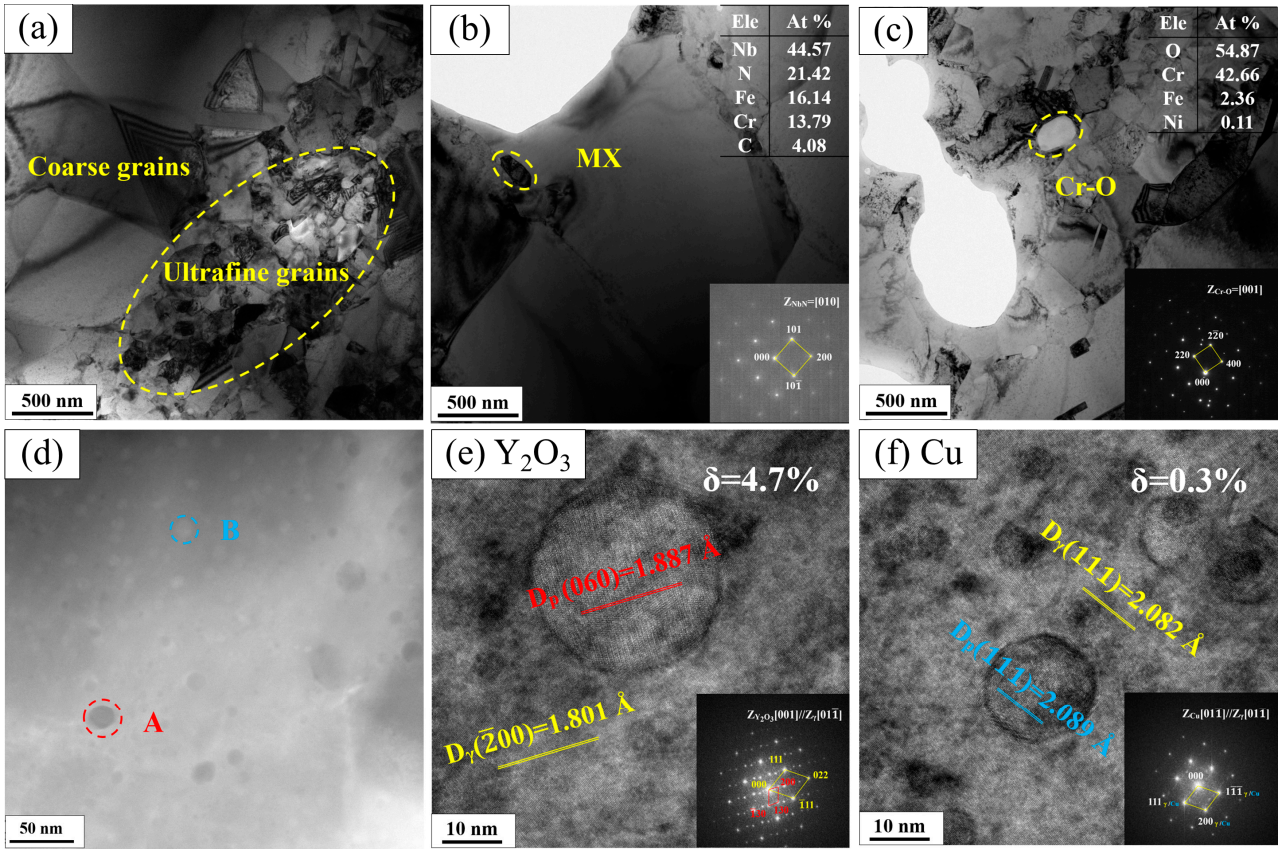



**Figure 3.** TEM image of (**a**) grains in the as-HIPed austenitic ODS steel, (**b**) MX nitrides (NbN), (**c**) Cr-O oxides; (**d**) HAADF image of nanosized precipitates; HRTEM images of (**e**) $Y_2O_3$ and (**f**) Cu-rich nanoparticles, labelled as A and B in (**d**).

Furthermore, several types of precipitates can be found within the matrix. As can be seen, MX carbon-nitrides with a stable FCC structure are distributed along the grain boundaries (Figure 3b). These precipitates are identified as NbN particles, according to the selected area electron diffraction (SAED) and EDS results, and their mean diameter is about 0.29 μm. Some bright Cr-O particles preferentially precipitate within the UFG region, and their mean diameter is about 0.24 μm (Figure 3c). In addition, some disc-shaped nanoparticles that are dispersedly distributed can be observed within the austenite grain

interior (Figure 3d). The mean diameter of these particles is about 9.7 nm, and the number density is $2.6 \times 10^{15}$ $m^{-2}$. According to HAADF-STEM results, two kinds of nanoparticles (marked as A and B) can be identified in Figure 3d. Particle A, exhibiting stronger contrast with the matrix, due to its heavier molar mass, is identified as $Y_2O_3$ phase (Figure 3e), and Particle B is characterized as Cu-rich phase (Figure 3f). The lattice misfits ($\delta$) of the $Y_2O_3$ and Cu-rich phases with the austenite matrix can be quantified by the following formula [23]:

$$\delta = 2\frac{|D_m - D_p|}{D_m + D_p} \quad (1)$$

where $D_m$ and $D_p$ represent the interplanar spacing of the mismatched planes in the matrix and particle, respectively. For the $Y_2O_3$ particle, the interfacial orientation relationships are determined as $[001]_{Y_2O_3}\left|\right|[01\bar{1}]_{Matrix}$ and $(200)_{Y_2O_3}\left|\right|(022)_{Matrix}$, and the value of $\delta$ is calculated as 4.7% (Figure 3e). As for the Cu-rich phase, the parallel zone axes are found to be $[01\bar{1}]_{Cu}||[01\bar{1}]_{Matrix}$, with a pair of parallel planes of $(111)_{Cu}||(111)_{Matrix}$, and the value of $\delta$ is merely 0.3% (Figure 3f). Both kinds of particles exhibit a completely coherent relationship with the austenite matrix, which is favorable for their precipitation. These coherent nanoparticles can effectively obstruct the motion of dislocations and the migration of grain boundaries during creep, contributing to the microstructure stability of the austenitic ODS steel.

### *3.2. Creep Behavior*

Figure 4a,b present the creep strain versus time curves and creep rate versus time curves under 100–300 MPa at 650 °C, respectively. It can be found that, with the increase of applied stress, the creep rupture time decreases, and the minimum creep rate increases. In detail, the creep rupture time is shortened from 4572.53 to 1.89 h, and the minimum creep rate increases from $4.48 \times 10^{-4}$ to 0.77 $h^{-1}$. This can be attributed to the higher stress levels during the creep period, which can accelerate the deformation rate and cause premature failure. When the applied stress is higher than 195 MPa, the creep strain increases with the increase of stress. However, it should be noticed that creep strain under 100 MPa (4.29%) is higher than that under 300 MPa (2.40%). This can be attributed to the extremely slow deformation rate under low stress levels, which leaves enough time for the recovery behavior to alleviate the working hardening effect, thus promoting continuous deformation in return. In general, a relatively short gauge length is prone to lead to an amplified overall creep strain [24,25], but it has no noticeable effect on other creep characteristics, such as creep strength and failure mode. Therefore, the obtained creep results are reliable in revealing the creep deformation behavior of the Super304H ODS steel. The detailed creep properties under different stress levels, involving creep strain ($\varepsilon_f$), creep rupture time ($t_r$), and the minimum creep rate ($\dot{\varepsilon}_m$), are statistically summarized in Table 2.

**Table 2.** Detailed creep properties of the Super304H ODS steel under different stress levels at 650 °C.

| **Stress (σ, MPa)** | **100** | **195** | **230** | **265** | **300** |
|---|---|---|---|---|---|
| **Creep strain ($\varepsilon_f$, %)** | 4.29 | 0.80 | 1.31 | 1.85 | 2.40 |
| **Creep rupture time ($t_r$, h)** | 4572.53 | 12.59 | 7.41 | 3.45 | 1.89 |
| **Minimum creep rate ($\dot{\varepsilon}_m$, $h^{-1}$)** | $4.48 \times 10^{-4}$ | 0.0415 | 0.1297 | 0.3302 | 0.7677 |

The creep deformation mechanism of the austenitic ODS steel is analyzed through the relationship between the minimum creep rate ($\dot{\varepsilon}_m$) and applied stress (σ), based on the Norton's power law [26]:

$$\dot{\varepsilon}_m = B\sigma^n \quad (2)$$

where $B$ is a constant, and $n$ is the stress exponent to represent different mechanisms of creep deformation. However, it should be noted that, in the ODS steel, the dispersed distribution of precipitates can effectively impede the dislocation motions, displaying

threshold stress [27,28]. Hence, the $n$ discussed here actually presents the apparent stress exponent. Figure 5 displays the double logarithmic curve of the minimum creep rate versus stress. The line is well-matched across varied stresses, demonstrating an identical creep deformation mechanism under different stresses. The apparent stress exponent $n$ is calculated to be 6.7, which is close to that reported in 18Cr9Ni and 316LN austenitic stainless steels [26,29]. This suggests that the creep deformation of the Super304H ODS steel is controlled by dislocation motion [30].

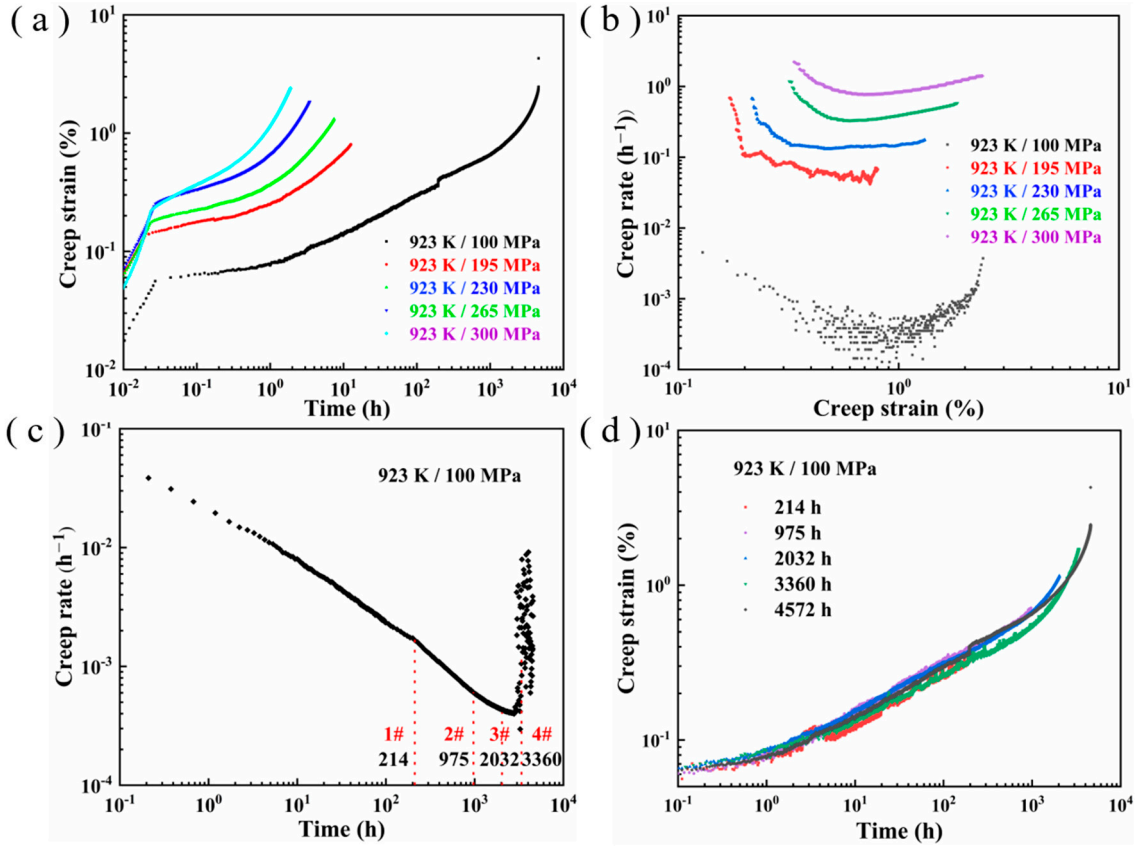



**Figure 4.** (**a**) Creep strain versus time curves, (**b**) creep rate versus creep strain curves, (**c**) creep rate versus time curve under 100 MPa, and (**d**) creep strain versus time curves for interrupted samples.

To further clarify the microstructure evolution at different creep stages, creep tests for interrupted samples were carried out under 100 MPa, and the results are shown in Figure 4c. As can be seen, the whole creep period can be divided into three distinct creep stages: the transient creep stage with gradually decreasing creep rate, the steady-state creep stage with a stable creep rate, and the accelerated creep stage with rapidly increasing creep rate. On account of this, the interrupted time was set as 214, 975, 2032, and 3360 h, on behalf of the transient stage, the early steady-state stage, the medium steady-state stage, and the onset of the accelerated stage, respectively. Figure 4d presents the corresponding creep strain versus time curves. It can be found that all interrupted creep curves fit well with that of the fracture sample, suggesting the good repeatability of creep tests and the uniform microstructure distribution of this austenitic ODS steel.

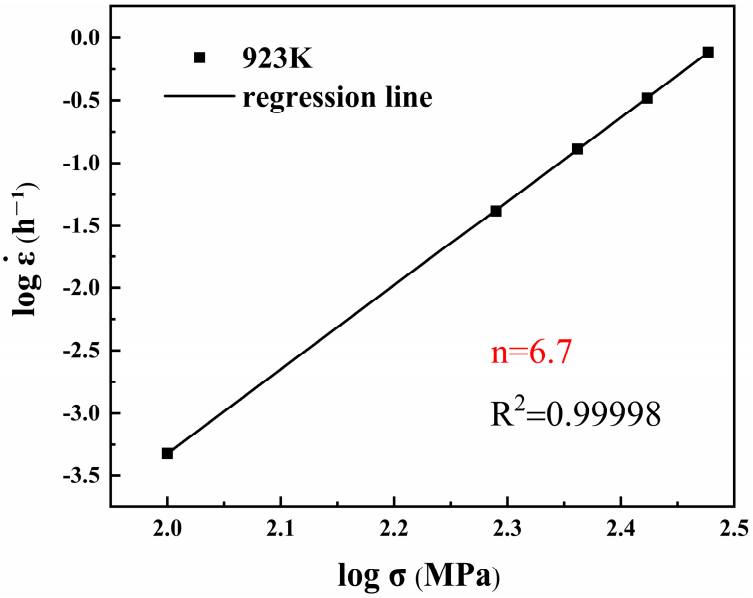



**Figure 5.** Relationship between the minimum creep rate and the applied stress of the Super304H ODS steel at 650 °C.

### *3.3. Microstructure and Microhardness Evolution during Creep*

#### 3.3.1. Evolution of Precipitates

Figure 6 presents the evolution of MX phases, Cr-O oxides, and $M_{23}C_6$ particles during different creep stages, and Figure 7 presents the corresponding mean diameters and particle density, which means the number of particles per unit area. As mentioned above, in the Super304H austenitic ODS steel, MX phases and Cr-O oxides dispersedly precipitate within the grain interior during the HIP process (Figure 2b,c). In addition, $M_{23}C_6$ carbides are found to precipitate along austenite grain boundaries during creep.

As shown in Figure 6a–c, with the prolongation of the creep period, the MX phases still exist within the grain interior in square or bulk shapes. The mean diameter of them remains stable, and the particle density gradually decreases (Figure 7). Prat et al. have stated that MX phases possess excellent thermal stability, thus leading to a lower coarsening rate [31]. In addition, it has also been proved that the main role of MX particles in contributing to creep strength is impeding the dislocation motions during creep, and the interactions between dislocations could accelerate the dissolution of MX phases, thus resulting in the decrease of number density [32].

As shown in Figure 6d–f, with the prolongation of the creep period, Cr-O oxides remain in a round shape and are prone to precipitate within the fine-grain region. As the creep time is prolonged to 2032 h, the particle density of Cr-O phases increases from ~0.3 to ~0.35 $\mu m^{-2}$, and then remains stable (Figure 7). Notably, the preferential accumulation of these particles in the fine grain zone can induce stress concentration at the boundaries between UFG and MG, leading to the formation of creep cavities.

As shown in Figure 6g–i, $M_{23}C_6$ carbides precipitate in a bulk shape along grain boundaries during the early creep stages of 214 h, and then these particles transform into a chain-like shape. With the prolongation of the creep period, as shown in Figure 7, the mean diameter and particle density first present an increasing trend from 214 to 975 h, and then remain stable until 3360 h. After that, the $M_{23}C_6$ particles start to grow rapidly, resulting in a sharp decrease of particle density. The coarsening process is related to the diffusion of Cr atoms from austenite, where the grain boundaries can act as diffusion channels [33]. As a result, Cr-poor zones can be formed at the interface, weakening the matrix [30,33]. In addition, Wang et al. proved that the coarsening of $M_{23}C_6$ particles would weaken their pinning ability for boundary migrations, leading to the growth of grains [11].

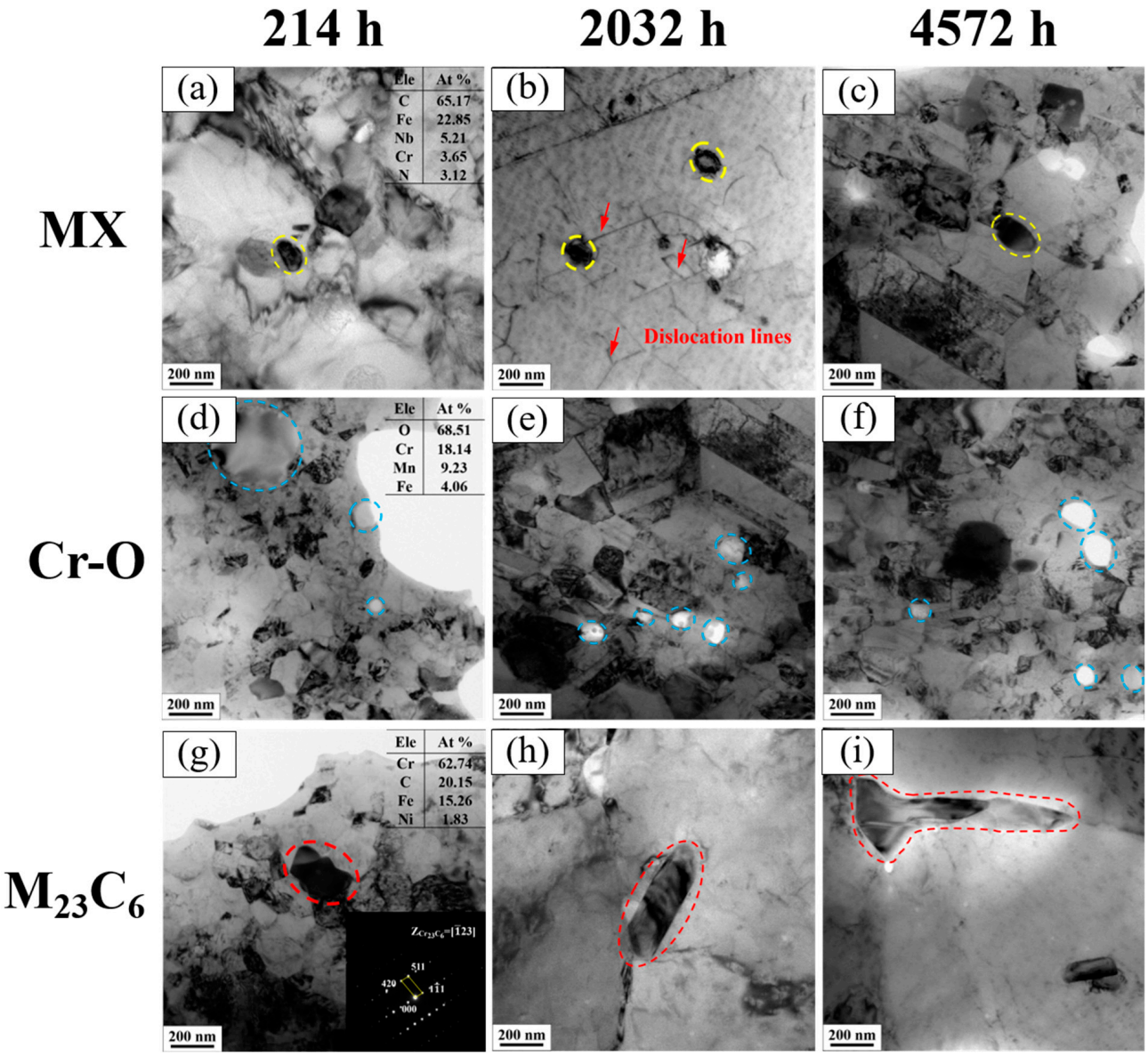



**Figure 6.** Submicron scale precipitates of the austenitic ODS steel during long-term creep: (**a**–**c**) MX carbides or nitrides, (**d**–**f**) Cr-O oxides, and (**g**–**i**) $M_{23}C_6$ carbides.

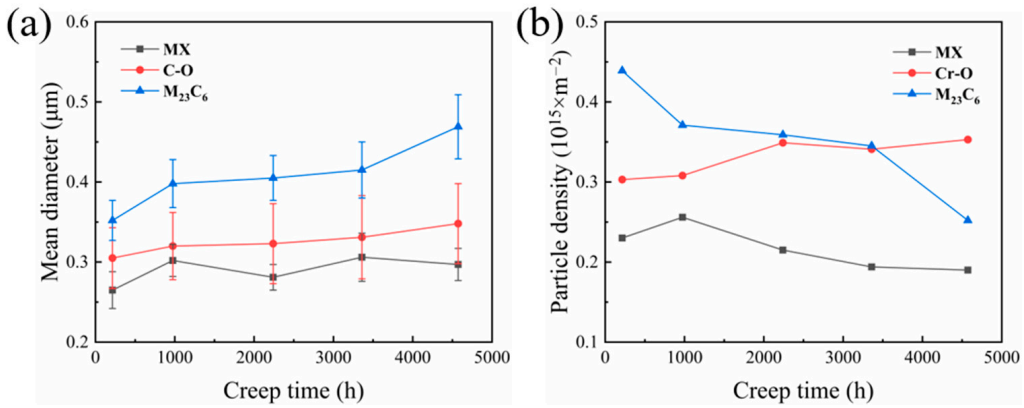



**Figure 7.** Variation curves of (**a**) mean diameter and (**b**) particle density of MX carbides or nitrides, Cr-O oxides, and $M_{23}C_6$ carbides, along with creep time.

Figure 8 presents the distribution of $Y_2O_3$ and Cu-rich phases and their interfacial relationship with the matrix after creep rupture. In HAADF-STEM images, the gray particles are $Y_2O_3$ phases, and the brighter particles are Cu-rich phases, due to their different atomic weight. As can be seen, the $Y_2O_3$ particle maintains a semi-coherent relationship with the matrix, and the lattice misfit is calculated to be 10.1%; Cu-rich particles still keep a completely coherent relationship with the matrix, and the lattice misfit $\delta$ is 1.2% (Figure 8b,c). Figure 9 displays the mean diameter and particle density of Cu-rich and $Y_2O_3$ particles. During the whole creep period, the mean diameter of the Cu-rich particles gradually increases from ~12.5 to ~25 nm, while that of the $Y_2O_3$ particles remains stable. Before 972 h, the density of Cu-rich particles is about 2.5 $\times$ $10^{15}$ $m^{-2}$, which then quickly decreases to less than 1 $\times$ $10^{15}$ $m^{-2}$ with the prolongation of creep time, up to 2032 h. In contrast, the density of $Y_2O_3$ particles exhibits a gradually decreasing trend.

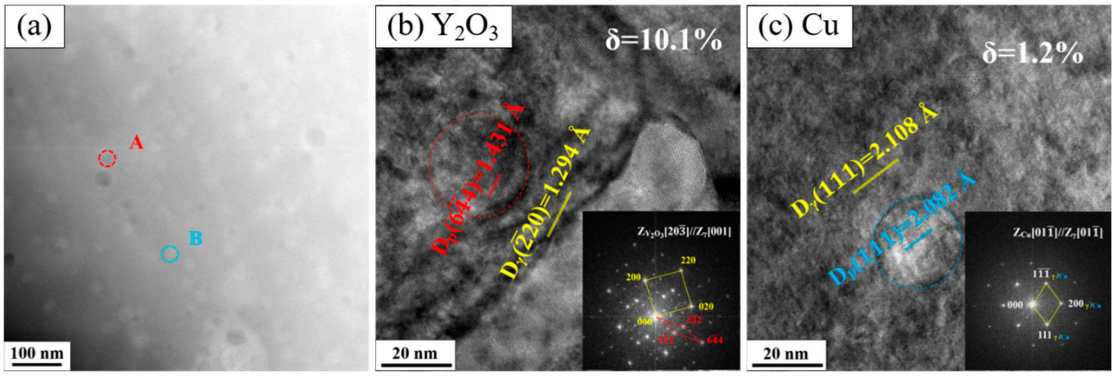



**Figure 8.** (**a**) HADDF image of nanoparticles in ruptured sample (where A and B represent different kinds of particles.); HRTEM images of (**b**) $Y_2O_3$ and (**c**) Cu-rich phase.

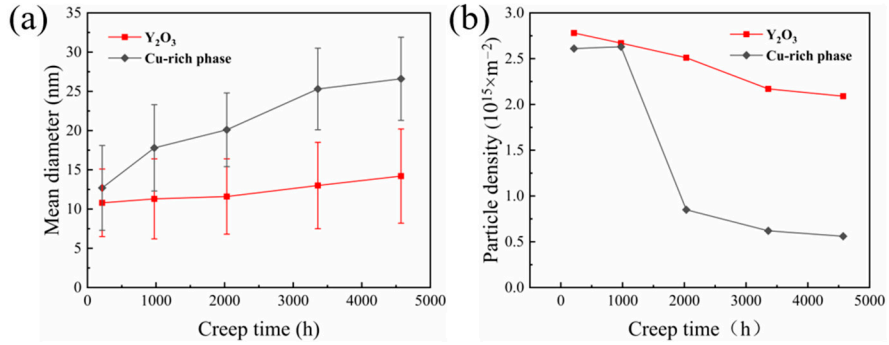



**Figure 9.** Variation curves of (**a**) mean diameter and (**b**) particle density of Cu-rich phases and $Y_2O_3$ phases with creep time.

Based on the above results, it can be recognized that $Y_2O_3$ particles exhibit superior thermal stability to Cu-rich phases. Cu-rich phases are typically soft particles, and can be easily dissolved into the matrix under the effect of dislocation cutting [15]. In addition, the completely coherent relationship with the matrix provides more diffusion channels for Cu atoms, which is beneficial for the growth of Cu-rich phases. Besides, $Y_2O_3$ particles have a strong pinning effect on dislocations, so that they can sustain a notable density and maintain good coherence with the matrix until creep rupture. From a performance viewpoint, semi-coherent particles with suitable size are preferred, because they are non-sheared and can increase the detachment stress for pinned dislocations [34]. Therefore, compared with Cu-rich phases, $Y_2O_3$ particles play a more durable contribution on improving the creep strength in the Super304H ODS steel.

3.3.2. Evolution of Grain Structure

Figure 10 shows the inverse pole figures (IPFs) of the Super304H ODS steel in the as-HIPed state and during different creep stages, and Figure 11 displays the corresponding grain size distribution histograms, where the red line is its fitting result through Gaussian function. It can be seen that the grain orientation in all samples is random, and no evident texture is formed during the whole creep process. Before creep, the UFG and CG zones can be clearly distinguished (Figure 10a). After creep for 214 h, the coarse grains are transformed into finer grains (Figure 10b). With the prolongation of creep period to 4572 h, the fine grains grow up, resulting in a gradually increasing percentage of the CG zone (Figure 10c–f).

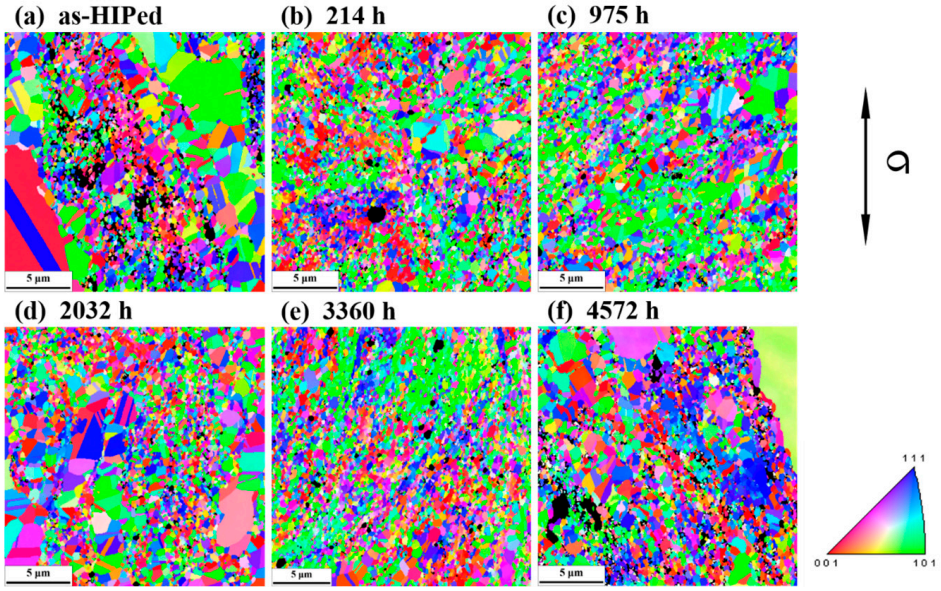



**Figure 10.** Inverse pole figure (IPF) of (**a**) as-HIPed sample, and samples for different creep stages: (**b**) 214 h, (**c**) 975 h, (**d**) 2032 h, (**e**) 3360 h, and (**f**) 4572 h.

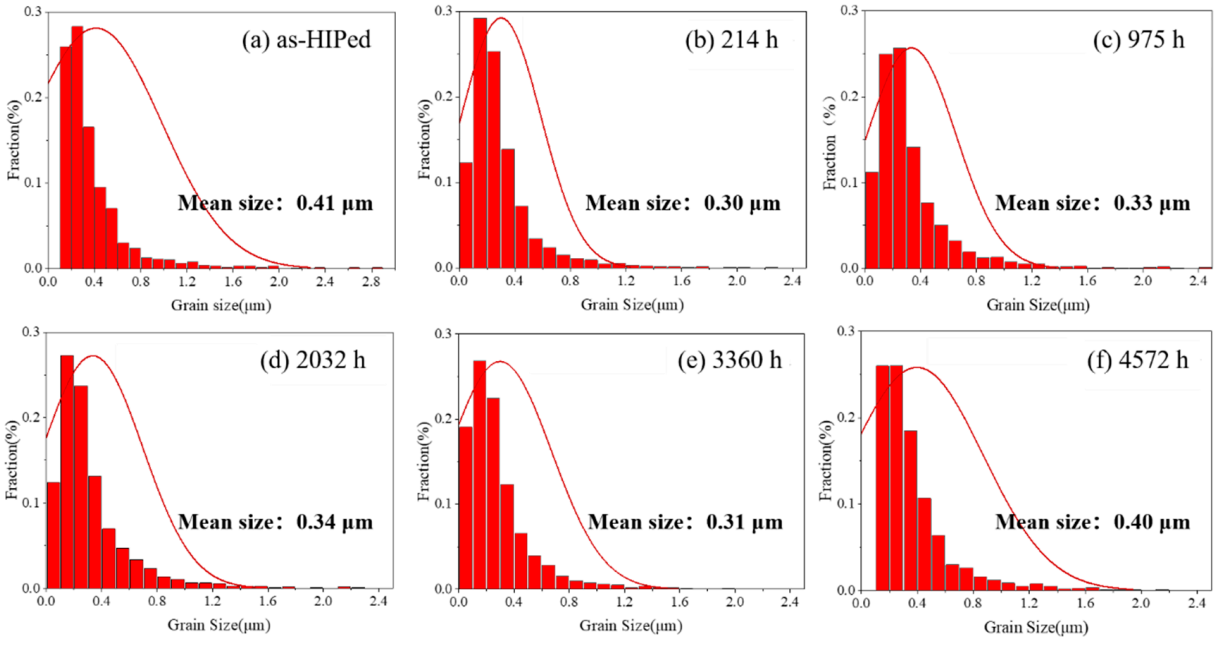



**Figure 11.** Statistical histograms of grain size distribution for (**a**) as-HIPed sample and samples in different creep stages: (**b**) 214 h, (**c**) 975 h, (**d**) 2032 h, (**e**) 3360 h, and (**f**) 4572 h.

In detail, compared with the as-HIPed state, the mean grain size is reduced from ~0.41 to ~0.30 μm during the initial 214 h, due to the dynamic recrystallization within the matrix (Figure 11a,b). This process involves the nucleation, growth, and replacement of grains in response to high-temperature plastic deformation. The entanglement of dislocations can create sites for the nucleation of new grains, which contributes to relieving deformation hardening [6]. During the second stage from 214 to 3360 h, the mean grain size is maintained at ~0.3 μm, on account of the work-hardening balance (Figure 11c–e). During the last stage, from 3360 to 4572 h, the mean grain size sharply increases from 0.31 to 0.40 μm, owing to the grain coarsening and the decrease of the number density of $M_{23}C_6$ particles, which weaken the pinning ability for boundary migrations (Figure 11f).

#### 3.3.3. Evolution of Microhardness

Figure 12 presents the evolution of microhardness of the Super304H ODS steel during the creep period. The hardness value increases from 273.6 ± 4.6 to 294.1 ± 5.9 HV during the first creep stage of 214 h. This can be attributed to the dynamic recrystallization behavior, which can produce numerous finer grains and enhance the boundary-hardening effect. With the prolongation of the creep period to 3360 h, the hardness gradually decreases to 286.5 ± 6.1 HV, indicating that the particle strengthening effect and matrix softening behavior are roughly kept in balance. Further, with the prolongation of creep time to 4572 h, the hardness exhibits a relatively fast decrease to 271.7 HV. This can be explained by the intense coarsening of $M_{23}C_6$ particles and the growth of grains, which weakens solution-hardening and boundary-hardening effects [11].

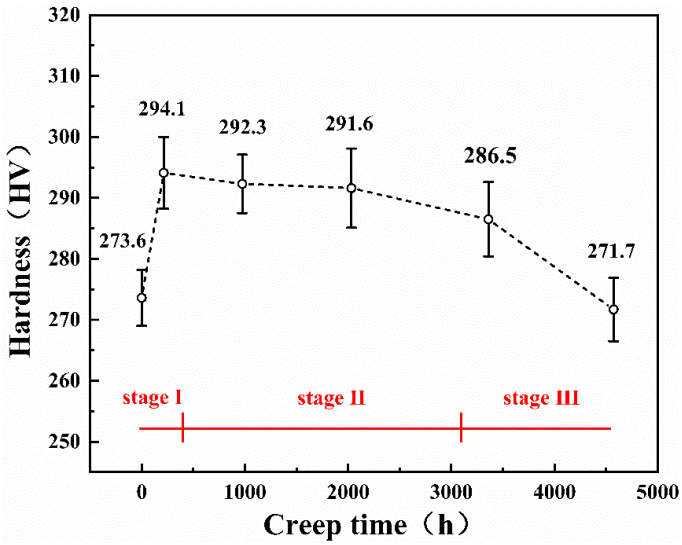



**Figure 12.** Evolution of microhardness during long-term creep.

It should be mentioned that there is no significant difference in microhardness between the ruptured sample and the as-HIPed one, indicating that the austenite matrix has not been significantly weakened after long-term creep.

### *3.4. Creep Damage and Fracture Mechanism*

Figure 13 depicts the creep damage images around the deformed zone during different creep stages of the Super304H ODS steel. When the creep time is 975 h, no obvious creep damage can be observed. As the creep time is extended to 2032 h, some creep cavities appear along grain boundaries (Figure 13a,b). With further prolongation of the creep period, the number density and size of creep cavities increase, causing contact with each other, leading to the formation of creep cracks (Figure 13c,d). Due to the incompatible deformation ability and the existence of Cr-O phases with higher hardness, the creep cavities are likely to form along the interfaces between the UFG and CG zones (Figure 13e). Additionally,

some coarse $M_{23}C_6$ particles are observed around the creep cracks. Hu et al. have proved that, during the creep deformation process, stress concentration can be generated around the interface between the precipitates and the matrix [18]. As the stress value exceeds the fracture critical stress, creep cavities start to nucleate and grow, eventually resulting in failure.

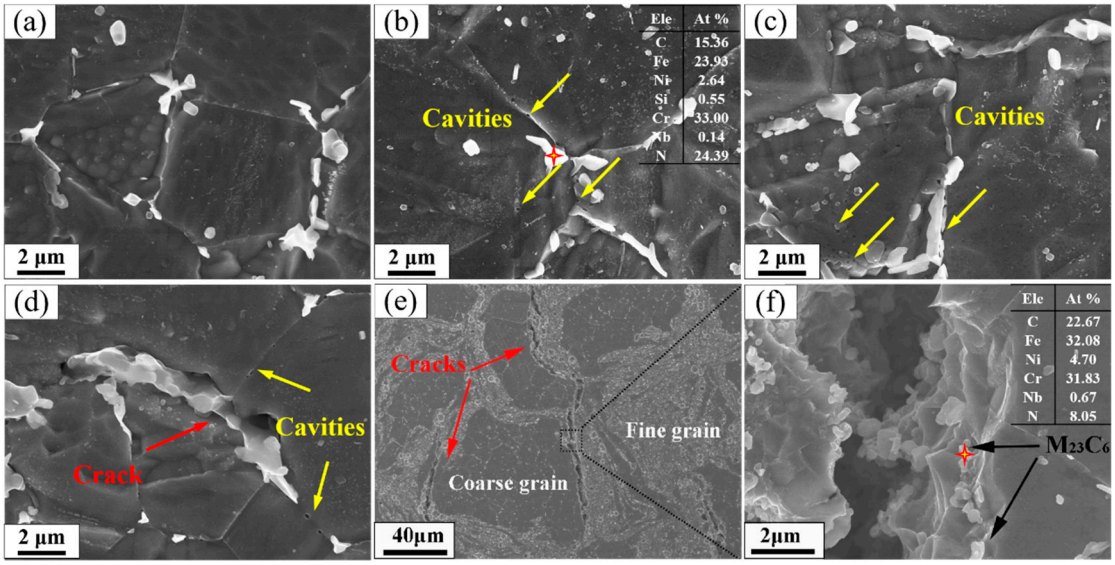



**Figure 13.** Cavity morphologies of austenitic ODS steel in the vertical direction during different creep stages: (**a**) 975 h, (**b**) 2032 h, (**c**) 3360 h, and (**d**) 4572 h; (**e**,**f**) Creep cracks in the longitudinal direction at 4572 h.

Figure 14 shows the fracture morphology after creep rupture of the Super304H ODS steel. It can be seen that only cleavage planes are generated on the fracture surface, suggesting a brittle fracture characteristic. In addition, some $M_{23}C_6$ carbides are also found near grain boundaries, indicating that these particles are the inducements for creep damages [15].

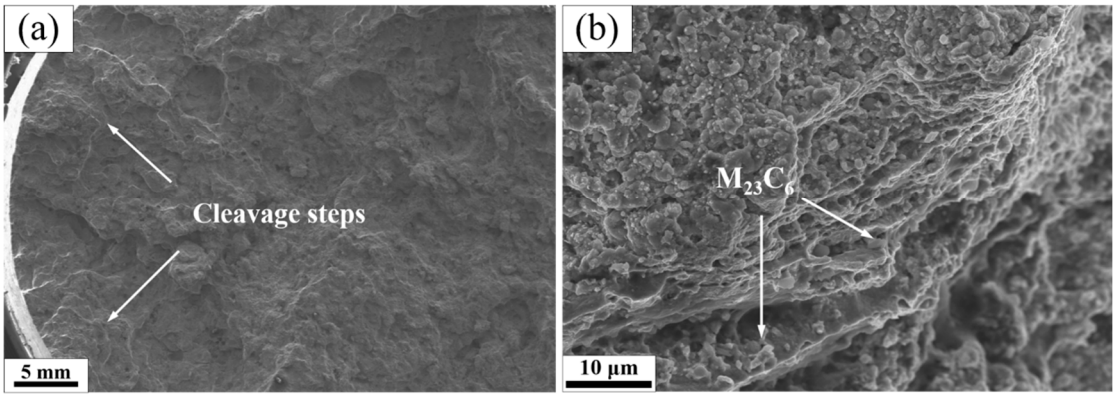



**Figure 14.** Creep fracture images at (**a**) a low magnification and (**b**) a higher magnification.

The creep damage tolerance factor ($\lambda$) proposed by Kachanov and Rabotnov can be used to analyze the creep damage mechanism, which can be expressed as follows [35]:

$$\lambda = \varepsilon_f / \dot{\varepsilon}_m t_r \quad (3)$$

where $\varepsilon_f$ is the fracture strain, $\dot{\varepsilon}_m$ is the minimum creep rate, and $t_r$ is the rupture time. In general, the value of $\lambda$ for different steels varies from 1 to 20; with the increase of $\lambda$ value, there is a gradual transition of the fracture mode from brittle fracture to ductile fracture.

Specifically, when $\lambda$ is 1, the fracture mode is determined to be a brittle fracture with a relatively low creep strain; when the value of $\lambda$ is in the range of 1.5–2.5, the creep damage mode is characterized by cavity growth; when $\lambda$ exceeds 2.5, the dominant damage mode is shifted to necking because of microstructure degradation.

Figure 15 exhibits the damage diagnostic diagram of the Super304H ODS steel under different stress levels. As can be observed, the values of $\lambda$ under different stress levels mostly fall into the range of void growth, indicating that the creep damage mode is cavity growth controlled by power law and diffusion creep. This phenomenon should be attributed to the combined effects of multiple factors, including grain deformation and precipitation coarsening, as well as the formation and growth of cavities. As described in Figure 12b, small cavities can form around $M_{23}C_6$ particles during the steady-state creep stage, and can gradually develop into creep cracks under continuously applied stress, finally leading to a premature rupture.

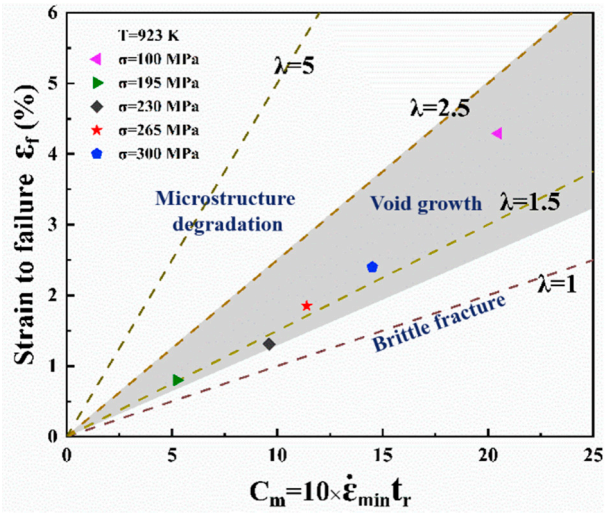



**Figure 15.** Damage diagnostic diagram of Super304H ODS steel at 650 °C.

## 4. Conclusions

In summary, the creep deformation behavior, microstructure evolution, and creep damage mechanism of Super304H ODS steel under different stress levels at 650 °C were investigated in this paper. The following conclusions can be drawn:

(1) The creep deformation behavior under different stress levels is studied. The apparent stress exponent $n$ is 6.7, which indicates that the creep deformation mechanism of Super304H ODS steel is dominated by dislocation motion.

(2) The microstructure evolution during long-term creep deformation is studied through interrupted creep experiments under 100 MPa. Along with creep, the austenite undergoes dynamic recrystallization, and $M_{23}C_6$ particles precipitate at grain boundaries, which can improve the microhardness during the first creep stage. Both $Y_2O_3$ and Cu-rich particles exhibit good coherence with the matrix, whereas $Y_2O_3$ precipitates are more important to creep strength because of their better thermal stability.

(3) The creep damage mode is determined as cavity growth, which is related to the coarsening of $M_{23}C_6$ particles and inhomogeneous stress distribution at grain boundaries.

**Author Contributions:** Conceptualization, W.Z. and L.Y.; methodology, W.Z. and L.Y.; validation, H.L.; formal analysis, W.Z.; investigation, W.Z. and Z.Z.; data curation, W.Z.; writing—original draft preparation, W.Z.; writing—review and editing, Z.Z., D.L., H.L. and L.Y.; supervision, L.Y.; project administration, L.Y.; funding acquisition, D.L. and L.Y. All authors have read and agreed to the published version of the manuscript.

**Funding:** This work was financially supported by the National Natural Science Foundation of China (Nos. U1960204 and 51974199).

**Data Availability Statement:** Not applicable.

**Acknowledgments:** The authors are grateful to the National Natural Science Foundation of China (Nos. U1960204 and 51974199).

**Conflicts of Interest:** The authors declare that they have no known competing financial interest or personal relationships that could have appeared to influence the work reported in this paper.

## References

1. Chi, C.-y.; Yu, H.-y.; Dong, J.-x.; Liu, W.-q.; Cheng, S.-c.; Liu, Z.-d.; Xie, X.-s. The precipitation strengthening behavior of Cu-rich phase in Nb contained advanced Fe–Cr–Ni type austenitic heat resistant steel for USC power plant application. *Prog. Nat. Sci. Mater. Int.* **2012**, *22*, 175–185. [CrossRef]
2. Vinoth Kumar, M.; Balasubramanian, V.; Gourav Rao, A. Hot tensile properties and strain hardening behaviour of Super 304HCu stainless steel. *J. Mater. Res. Technol.* **2017**, *6*, 116–122. [CrossRef]
3. Bai, J.W.; Liu, P.P.; Zhu, Y.M.; Li, X.M.; Chi, C.Y.; Yu, H.Y.; Xie, X.S.; Zhan, Q. Coherent precipitation of copper in Super304H austenite steel. *Mater. Sci. Eng. A* **2013**, *584*, 57–62. [CrossRef]
4. Zhou, Q.; Liu, J.; Gao, Y. An insight into oversaturated deformation-induced sigma precipitation in Super304H austenitic stainless steel. *Mater. Des.* **2019**, *181*, 108056. [CrossRef]
5. Song, G.D.; Hwang, J.H.; Kim, D.-W.; Park, B.C.; Hahn, J.; Hong, S.-G. Coexistence of two distinct fatigue failure mechanisms in Super304H welded joint at elevated temperatures. *Mater. Sci. Eng. A* **2021**, *819*, 141465. [CrossRef]
6. Huang, X.; Zhou, Q.; Wang, W.; Sheng Li, W.; Gao, Y. Microstructure and property evolutions of a novel Super304H steel during high temperature creeping. *Mater. High Temp.* **2017**, *35*, 438–450. [CrossRef]
7. Jiang, J.; Zhu, L. Strengthening mechanisms of precipitates in S30432 heat-resistant steel during short-term aging. *Mater. Sci. Eng. A* **2012**, *539*, 170–176. [CrossRef]
8. Ou, P.; Li, Z. Ordering of Primary Carbonitrides in an Austenitic Steel Revealed by Transmission Electron Microscopy and Atom Probe Tomography. *Materials* **2018**, *11*, 2321. [CrossRef]
9. Zieliński, A.; Golański, G.; Sroka, M.; Dobrzański, J. Estimation of long-term creep strength in austenitic power plant steels. *Mater. Sci. Technol.* **2016**, *32*, 780–785. [CrossRef]
10. Hwang, J.H.; Song, G.D.; Kim, D.-W.; Huh, Y.-H.; Park, B.C.; Hahn, J.; Hong, S.-G. Tensile and fatigue properties of Super304H welded joint at elevated temperatures. *Int. J. Fatigue* **2021**, *143*, 105989. [CrossRef]
11. Wang, X.; Li, Y.; Chen, D.; Sun, J. Precipitate evolution during the aging of Super304H steel and its influence on impact toughness. *Mater. Sci. Eng. A* **2019**, *754*, 238–245. [CrossRef]
12. Miao, Y.; Mo, K.; Zhou, Z.; Liu, X.; Lan, K.-C.; Zhang, G.; Miller, M.K.; Powers, K.A.; Almer, J.; Stubbins, J.F. In situ synchrotron tensile investigations on the phase responses within an oxide dispersion-strengthened (ODS) 304 steel. *Mater. Sci. Eng. A* **2015**, *625*, 146–152. [CrossRef]
13. Oka, H.; Watanabe, M.; Hashimoto, N.; Ohnuki, S.; Yamashita, S.; Ohtsuka, S. Morphology of oxide particles in ODS austenitic stainless steel. *J. Nucl. Mater.* **2013**, *442*, S164–S168. [CrossRef]
14. Wang, M.; Zhou, Z.; Sun, H.; Hu, H.; Li, S. Effects of plastic deformations on microstructure and mechanical properties of ODS-310 austenitic steel. *J. Nucl. Mater.* **2012**, *430*, 259–263. [CrossRef]
15. Leo, J.R.O.; Pirfo Barroso, S.; Fitzpatrick, M.E.; Wang, M.; Zhou, Z. Microstructure, tensile and creep properties of an austenitic ODS 316L steel. *Mater. Sci. Eng. A* **2019**, *749*, 158–165. [CrossRef]
16. Zhao, Q.; Yu, L.; Liu, Y.; Huang, Y.; Ma, Z.; Li, H.; Wu, J. Microstructure and tensile properties of a 14Cr ODS ferritic steel. *Mater. Sci. Eng. A* **2017**, *680*, 347–350. [CrossRef]
17. Peng, Y.; Yu, L.; Liu, Y.; Ma, Z.; Li, H.; Liu, C.; Wu, J. Microstructures and tensile properties of an austenitic ODS heat resistance steel. *Mater. Sci. Eng. A* **2019**, *767*, 138419. [CrossRef]
18. Hu, Z.-F.; Zhang, Z. Investigation the effect of precipitating characteristics on the creep behavior of HR3C austenitic steel at 650 °C. *Mater. Sci. Eng. A* **2019**, *742*, 451–463. [CrossRef]
19. He, H.; Zhang, J.; Yu, L.; Gao, Q.; Liu, C.; Ma, Z.; Li, H.; Liu, Y.; Wang, H. Effects of Cu-rich phases on microstructure evolution and creep deformation behavior of a novel martensitic heat-resistant steel G115. *Mater. Sci. Eng. A* **2022**, *855*, 143937. [CrossRef]
20. Ren, J.; Yu, L.; Liu, C.; Ma, Z.; Li, H.; Wang, Z.; Liu, Y.; Wang, H. Creep properties, microstructural evolution, and fracture mechanism of an Al added high Cr ODS steel during creep deformation at 600 °C. *J. Nucl. Mater.* **2022**, *558*, 153376. [CrossRef]
21. Koncz, P.; Horváth, Á.; Balázsi, K.; Şahin, F.Ç.; Göller, G.; Onüralp, Y.; Balázsi, C. Correlation between Milling Parameters, Structural and Mechanical Properties of Nanostructured Austenitic $Y_2O_3$ Strengthened Steels. *Mater. Sci. Forum* **2012**, *729*, 409–414. [CrossRef]
22. Wang, M.; Zhou, Z.; Sun, H.; Hu, H.; Li, S. Microstructural observation and tensile properties of ODS-304 austenitic steel. *Mater. Sci. Eng. A* **2013**, *559*, 287–292. [CrossRef]
23. Neumeier, S.; Pyczak, F.; Göken, M. The temperature dependent lattice misfit of rhenium and ruthenium containing nickel-base superalloys—Experiment and modelling. *Mater. Des.* **2021**, *198*, 109362. [CrossRef]
24. Zhao, Y.; Guo, Y.; Wei, Q.; Dangelewicz, A.; Xu, C.; Zhu, Y.; Langdon, T.; Zhou, Y.; Lavernia, E. Influence of specimen dimensions on the tensile behavior of ultrafine-grained Cu. *Scr. Mater.* **2008**, *59*, 627–630. [CrossRef]

25. Kiener, D.; Grosinger, W.; Dehm, G.; Pippan, R. A further step towards an understanding of size-dependent crystal plasticity: In situ tension experiments of miniaturized single-crystal copper samples. *Acta Mater.* **2008**, *56*, 580–592. [CrossRef]
26. Latha, S.; Mathew, M.D.; Parameswaran, P.; Bhanu Sankara Rao, K.; Mannan, S.L. Thermal creep properties of alloy D9 stainless steel and 316 stainless steel fuel clad tubes. *Int. J. Press. Vessel. Pip.* **2008**, *85*, 866–870. [CrossRef]
27. Ukai, S.; Mizuta, S.; Fujiwara, M.; Okuda, T.; Kobayashi, T. Development of 9Cr-ODS Martensitic Steel Claddings for Fuel Pins by means of Ferrite to Austenite Phase Transformation. *J. Nucl. Sci. Technol.* **2002**, *39*, 778–788. [CrossRef]
28. Arzt, E.; Wilkinson, D.S. Threshold stresses for dislocation climb over hard particles: The effect of an attractive interaction. *Acta Metall. Sin.* **1986**, *34*, 1893–1898. [CrossRef]
29. Praveen, C.; Christopher, J.; Ganesan, V.; Reddy, G.V.P.; Sasikala, G.; Albert, S.K. Constitutive modelling of transient and steady state creep behaviour of type 316LN austenitic stainless steel. *Mech. Mater.* **2019**, *137*, 103122. [CrossRef]
30. Sakthivel, T.; Selvi, S.P.; Laha, K. An assessment of creep deformation and rupture behaviour of 9Cr–1.8W–0.5Mo–VNb (ASME grade 92) steel. *Mater. Sci. Eng. A* **2015**, *640*, 61–71. [CrossRef]
31. Prat, O.; Garcia, J.; Rojas, D.; Carrasco, C.; Kaysser-Pyzalla, A.R. Investigations on coarsening of MX and M23C6 precipitates in 12% Cr creep resistant steels assisted by computational thermodynamics. *Mater. Sci. Eng. A* **2010**, *527*, 5976–5983. [CrossRef]
32. Tamura, M.; Sakasegawa, H.; Kohyama, A.; Esaka, H.; Shinozuka, K. Effect of MX type particles on creep strength of ferritic steel. *J. Nucl. Mater.* **2003**, *321*, 288–293. [CrossRef]
33. Godec, M.; Skobir Balantic, D.A. Coarsening behaviour of M23C6 carbides in creep-resistant steel exposed to high temperatures. *Sci. Rep.* **2016**, *6*, 29734. [CrossRef] [PubMed]
34. Arzt, E. Creep of oxide-dispersion strengthened alloys. In *Encyclopedia of Materials: Science and Technology*; Elsevier: Amsterdam, The Netherlands, 2001; pp. 1800–1806. [CrossRef]
35. Dyson, M.F.A.B.F. Creep Damage Mechanics and Micromechanisms. In Proceedings of the 6th International Conference on Fracture, New Delhi, India, 4–10 December 1984; pp. 1–29. [CrossRef]


**Disclaimer/Publisher's Note:** The statements, opinions and data contained in all publications are solely those of the individual author(s) and contributor(s) and not of MDPI and/or the editor(s). MDPI and/or the editor(s) disclaim responsibility for any injury to people or property resulting from any ideas, methods, instructions or products referred to in the content.